INHERENT INSENSITIVITY TO RF INHOMOGENEITY IN FLASH IMAGING

A Thesis
Presented to
The Academic Faculty

by

Danli Wang

In Partial Fulfillment
of the Requirements for the Degree
Master of Science in the
Department of Biomedical Engineering
in the College of Engineering

Georgia Institute of Technology
December 2003

ABSTRACT

MRI as a non-invasive method for studying the internal structure and function of the human body was developed over the past three decades. In MRI, radiofrequency (RF) field inhomogeneity is an unavoidable problem in practice and becomes severe at high magnetic fields due to the dependence of B_1 on the sample. It leads to nonuniformities in image intensity and contrast, causing difficulties in quantitative interpretation and image segmentation. In this thesis, we report an interesting observation that the fast low-angle shot (FLASH) sequence, which is often used for anatomic imaging and morphometric studies, can be insensitive to RF inhomogeneity when the same coil is used for both transmission and reception and a proper nominal flip angle is employed. Recommendations also are given for optimum processing procedures for FLASH imaging. This observation can be useful in understanding the signal behavior of FLASH in the presence of RF inhomogeneity and provides a guide for selecting parameters in FLASH imaging.

ACKNOWLEDGMENTS

I would like to thank my academic advisor, Dr. Xiaoping Hu, at School of Biomedical Engineering, to whom I am extremely honored and grateful for giving me the opportunity to join Biomedical Imaging Technology Center in the Fall of 2002. He never ceases to inspire me with new research ideas and provide me with numerous opportunities to expand my knowledge about magnetic resonance imaging. Without his help, I would not have made the rapid progress demonstrated in this research.

Here at Gatech, I would like to thank the faculty and staff in the Biomedical Engineering Department. Specifically, I would like to thank Dr. Paul Benkeser who always squeezed his precious time to help me whenever I encountered any problems for my study with his unbelievable patience. I am especially grateful for his encouragement. This work is the culmination of his trust in me. I hope that I have made him proud.

I also wish to thank Dr. John Oshinski, who is full of knowledge and experience of MRI technology. I appreciate his helpful advice and encouragement on my study and research. It was my pleasure to have Dr. Oshinski on my committee.

Many thanks go out to all my colleagues and friends at Gatech who are such warm and congenial folks. I wish to thank Dr. Stephen LaConte, Dr. Keith Heberlein and Dr. Yasser Kadah, for giving me a lot of help to troubleshoot the previously unstable

instruments. Special thanks go to Ms. Jane Chisholm working at Gatech language institute for her kindness and help on my writing. One sentence is not enough to express my thanks for all their wonderful work on my thesis.

My deepest thanks go to my parents in P. R. China, whose moral support and encouragement have been invaluable in giving me the confidence to come this far. Finally, heartfelt thanks go to my wife, Huijun, to whom this thesis is dedicated. I do not know how to thank you enough for helping me stay focused on my work, and making me stronger.

This work is supported by NIH grants RO1MH55346 and RO1EB00321, the Georgia Research Alliance, and the Whitaker Foundation.

TABLE OF CONTENTS

LIST OF FIGURES

LIST OF TABLES

1. INTRODUCTION

1.1 Medical imaging background

The brain is the most fascinating, and least understood, organ in the human body. For centuries, scientists and physicians have pondered the structure and function of the brain. The impact of medical imaging on understanding the brain has been considerable. The advent of x-ray computed tomography (CT) in the 1970's allowed clinicians to see features inside the heads of patients without the need for surgery. Since a positron almost immediately annihilates with an electron, choosing to use a positron emitter as the radioisotope forward made a big step that now not only structure but also blood flow and metabolism could be measured [1]. Using labeled water, positron emission tomography (PET) became the first useful technique that allowed researchers to produce maps of the mind, by measuring blood flow during execution of simple cognitive tasks.

At around the same time, another technique that promised even better anatomical details of the brain was being developed. By placing the body in a strong magnetic field and measuring how different tissues respond to a radiofrequency (RF) pulse, a magnetic resonance imaging (MRI), based on the phenomenon of nuclear magnetic resonance, produces images of the brain, allowing physicians to distinguish between gray and white matter, and brain defects such as tumors. Since MRI involves no ionizing radiation, the

risks to the subject are minimized. There are many inherent advantages for MRI. One of important advantages is that MRI generates three-dimensional grid of sample points which captures not just the visible outer surface of the body, but its internal structures with different contrast among soft tissues as well. As a non-invasive way for studying the internal structure and function of the human body, MRI was developed over the three decades by different government agencies, together with industries and universities from different countries. Figure 1 displays a typical clinical MRI scanner and a set of example of MR imaging of head. Current MRI technology offers sub-millimeter accuracy, and it will undoubtedly improve with time.

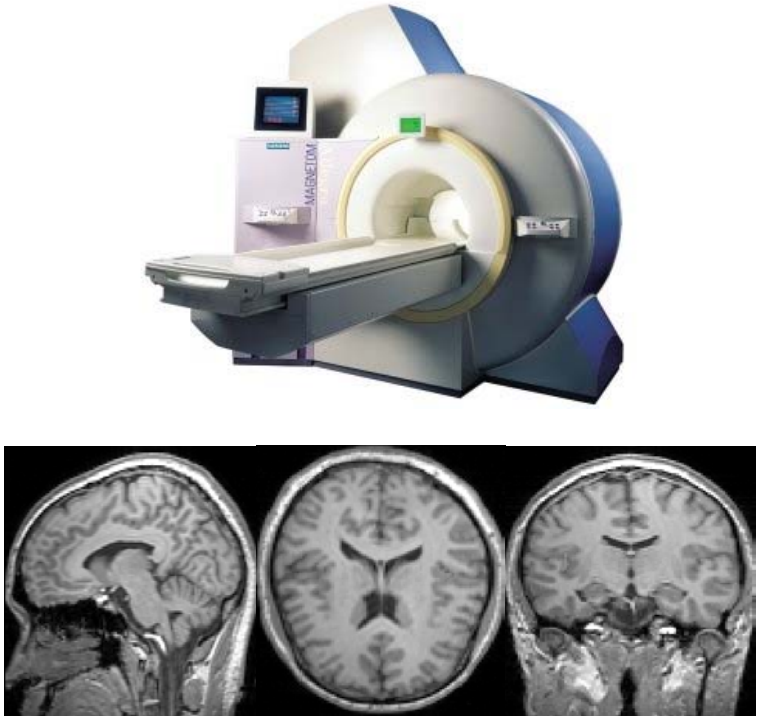

Figure 1: Typical clinical MRI Scanner and MR imaging of head (sagittal, transverse and coronal views)

1.2 Motivation and purpose of the work

In most cases, it is tacitly assume in MRI that the RF coil is perfect. However, due to practical constraints, the RF coil used in MRI cannot be built to generate a completely uniform RF field (B_1) or to have truly uniform reception sensitivity over the field of view (FOV). Nonuniform B_1 leads to a nonuniform flip angle (FA) which results in spatial variations in both contrast and intensity; nonuniformities in reception sensitivity cause image intensity variations. Consequently, RF coil nonuniformities can lead to significant spatial variations subsequent reduction in the measurement accuracy in the image contrast and intensity, making quantitative image interpretation and segmentation difficult. Because of the limitation of the signal-to-noise ratio (SNR) associated with low frequencies, it is desired to enhance SNR at a higher magnetic field. However, as the strength of the magnetic field increases, the frequency of the B_1 field increases linearly. For instance, the frequency of the B_1 field for a 4 Telsa system is 171 MHz for proton imaging. At such a high frequency, the interaction between the B_1 field and the human body can no longer be neglected. Such a strong interaction not only leads to further degradation of the RF uniformity [2-3] and thus the imaging quality, but also can cause concerns about the safety because the electric field associated with the B_1 field increases with the inhomogeneity of the B_1 field. Thus the problem of RF inhomogeneity is exacerbated at high magnetic fields.

1.3 Possible solutions

A number of investigators have pointed out the importance of correcting the B_1 inhomogeneity in tissue segmentation [4-6]. Some people put their efforts to try to improve the RF coil design and thus to reduce the B_1 inhomogeneity artifact [7-8]. However, it is hard to construct the RF coil to generate a completely uniform B_1 field because of practical constraints on coil design. Another common approach to ease the B_1 inhomogeneity effect is by using image post processing algorithms. Several methods have been developed using this approach [9-14]. While these methods have met with good success, they can be computationally intensive, do not account for contrast variations due to nonuniform excitation, and are mostly based on an approximation of the sensitivity field. More important, they are not easy carried out in all three dimensions. For example, a method designed based on spatially varying excitation was recently introduced for magnetization prepared ultrafast gradient-echo imaging and demonstrated to be highly effective for 2D imaging [15].

To date, most morphometric studies are based on high-resolution 3D T1-weighted images, often acquired with a 3D fast low-angle shot (FLASH) sequence [16] or a 3D magnetization-prepared rapid gradient-echo (MPRAGE) sequence [17]. While both sequences are being widely used, their performance in terms of image uniformity can be quite different because they are based on different physical principles. In particular, with adiabatic inversion as is commonly done, MPRAGE is monotonically affected by RF sensitivity in both excitation (for flip angles normally used) and reception while FLASH's dependence on RF sensitivity is not monotonic since its signal intensity has a

nonlinear dependence on flip angle. Such a difference may be significant at high magnetic fields, which are becoming widely accessible to the research and clinical community. This thesis reports an observation that 3D FLASH images obtained with a proper flip angle can be insensitive to coil inhomogeneity when the same coil is used for both transmission and reception. This observation provides a new understanding of the FLASH signal behavior in the presence of B_1 inhomogeneity and could be beneficial in MRI anatomic studies and facilitate automatic segmentation.

1.4 Organization of the Thesis

The material presented in this thesis covers a number of the aspects concerning a interesting observation that 3D FLASH sequence, which is often used for anatomic imaging and morphometric studies, can be insensitive to RF inhomogeneity when the same coil is used for both transmission and reception and a proper nominal flip angle is employed.

This thesis is organized into five chapters. Chapter 1 is the introduction. The second chapter reviews the basic principles of magnetic resonance imaging, including the classical and quantum mechanical descriptions of nuclear magnetic resonance. Chapter 3 is concerned primarily with our approach, including theory, method and computer simulation. Chapter 4 describes the measurement results. It includes a comparison between phantom and normal human volunteers. Chapter 5 summarized the conclusions of this thesis.

2. MRI PRINCIPLES

Medical magnetic resonance imaging (MRI) is a widely employed imaging technique for obtaining high-resolution anatomical and functional images of various organs within the human body by mapping the distribution of hydrogen nuclei. MRI is a non-invasive technique based on the same principles as nuclear magnetic resonance (NMR) in vivo. Bloch [18] and Purcell [19] independently discovered NMR in 1946. The process of acquiring two-dimensional MR image of a phantom by applying the Fourier transformation to raw NMR signal was first illustrated by Paul C. Lauterbur [20] in 1973. All of them were awarded the Nobel Prize for their achievements. The theory behind NMR is rather complicated and very comprehensive details of MRI can be found in [21-22]; what follows is a simplified summary of this theory.

2.1 Spin in a magnetic field

Nuclei with an odd number of protons and neutrons possess a property called spin. Nuclei spins can be visualized as a rotating motion of the nucleus about their own axis that create micro-magnetic fields around themselves, so that each nucleus resembles a tiny bar magnet with the north and south poles along the axis of spin. In the absence of an externally applied magnetic field, spins are oriented randomly so that there is no net

magnetic field. However, if spins are exposed to a strong and homogeneous external magnetic field (B_0), the spins will line up to create a detectable magnetic field. The alignment can be two possible states, a low energy (parallel) and a high energy (anti-parallel) state(see Figure 2).

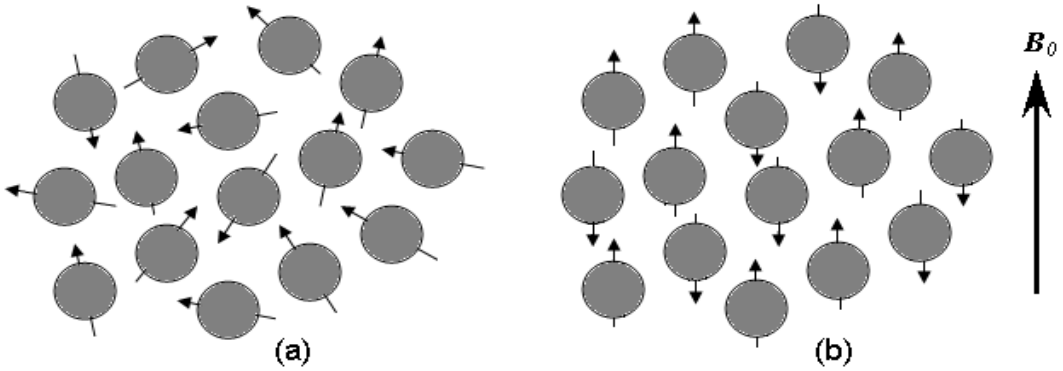

Figure 2: (a) In the absence of an externally applied magnetic field, a collection of spins is oriented randomly. (b) When an external magnetic field B_0 is applied, the spins will align themselves in one of two orientations with respect to B_0.

In addition, the spin axes are not exactly aligned with B_0 and each spin in the magnetic field precesses with a characteristic frequency known as the Larmor frequency, which is defined as:

$$\omega_0 = \gamma B_0 \tag{1}$$

where γ is the gyromagnetic constant. This is analogous to the motion of a spinning top precessing in the Earth's gravitational field. The gyromagnetic constant is a specific number for each different nuclear species. This means, for instance, that hydrogen nuclei ($\gamma \approx 42.58$ MHz/T) under a specified magnetic field will spin at a predictable frequency.

If the magnetic field changes, the spin frequency changes. Since biological material consists with abundance hydrogen nuclei (H_1), hydrogen imaging is the most widely used MRI procedure.

2.3 RF pulses

The concept of acquiring MRI is based on emitting RF wave in the presence of the magnetic field with strength B_0 in the z-direction. At magnetic equilibrium, there are more spins in the low energy state (E_1) than in the high energy state (E_2) at room temperature. Therefore, there will be a net magnetization M_0 in the longitudinal direction (the direction of the external magnetic field) after reaching equilibrium. This net magnetization can be represented as vectors, as shown in Figure 3. Every vector can be described by its components perpendicular to and parallel/anti-parallel to B_0. For a large enough number of spins, individual components perpendicular to B_0 cancel, leaving only components in the direction parallel/anti-parallel to B_0. As most spins adopt the parallel rather than the anti-parallel state, the net magnetization M_0 is in the direction of the B_0 field.

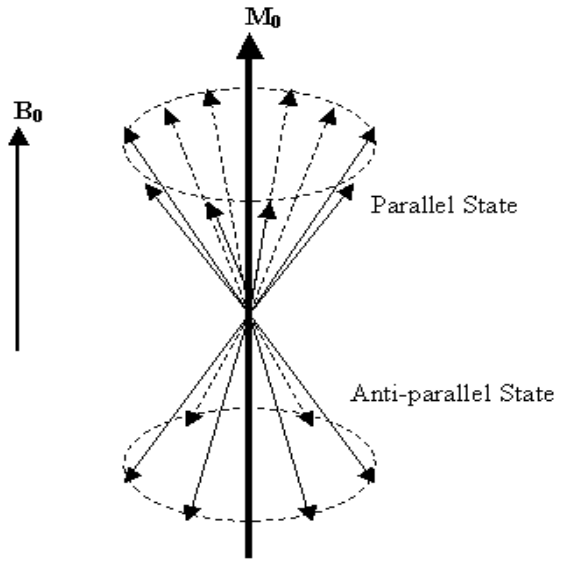

Figure 3: A net magnetization M_0 in the longitudinal direction (the direction of the external magnetic field) after reaching equilibrium.

Suppose the direction of B_0 is aligned with the z-axis. The plane perpendicular to B_0 contains the x and y-axes. When a RF pulse (electromagnetic wave) is applied perpendicularly to B_0 and it oscillates at the Larmor frequency, the spins absorb energy from the RF wave and are excited to a higher energy state. This phenomenon is referred to as resonance (see Figure 4). The x-y components of M_0 will be made coherent by the B_1 field giving a net x-y component to M and hence effectively causes M_0 to tilt from the z direction into the x-y plane. As soon as the RF pulse is switched off, the spins return to their equilibrium state and release absorbed energy to the environment as RF wave emissions. Sensors can then detect the emitted RF waves. This is the principle of NMR signal detection. It is from this received RF signal that an MR image can be constructed. The angle through which M has rotated away from the z-axis is known as the flip angle.

The strength and duration of B_1 determine the amount of energy available to achieve spin transitions between parallel and anti-parallel states. Thus, the flip angle is proportional to the strength and duration of B_1. The magnitude of the generated signal depends on the number of nuclei contributing to produce the transverse magnetization and on the relaxation times (see next section).

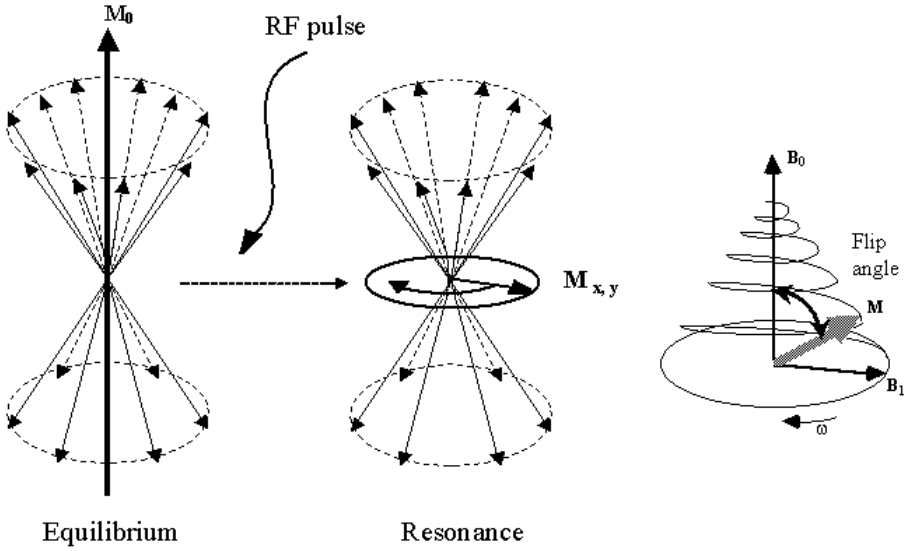

Figure 4: The effect of RF pulse on the net magnetization M_0. M_0 is tilted from its original longitudinal z-axis orientation, along the direction of the external magnetic field B_0, into the transverse x-y plane. An illustration of flip angle is the angle through which M has rotated away from the z-axis.

2.3 Relaxation Processes and MR signal

The process of M approaching its equilibrium (the direction of the z-axis) from an excited state is known as relaxation. The relaxation times are different for different kinds of tissue, which gives different intensities – contrasts – in the image. The relaxation can be characterized by two types: (1) spin-lattice relaxation: The spins exchange energy with

their surroundings to reach their previous equilibrium state in line with the constant external magnetic field B_0 (z-axis). This process is governed by the longitudinal relaxation time T_1 that is in its turn dependent on the tissue type. (2) Spin-spin relaxation: Spins experience, due to their surrounding spins, slightly different magnetic field strength such that their precessing frequencies vary over space. This leads to an internal dephasing of spins. During the dephasing process the spins lose their synchronicity and start spinning at different rate such that transverse magnetization decays over time. This kind of relaxation is parameterized by the transverse relaxation time T_2 (so known as T_2 decay), which is the decrease in the x-y component of magnetization. For the constant field, the dynamics of the magnetization components can be described by the Bloch equations as following:

$$\frac{dM_z}{dt} = \frac{M_0 - M_z}{T_1} \tag{2}$$

$$\frac{dM_x}{dt} = \omega_0 M_y - \frac{M_x}{T_2} \tag{3}$$

$$\frac{dM_y}{dt} = -\omega_0 M_x - \frac{M_y}{T_2} \tag{4}$$

where M_x, M_y, and M_z are the magnetization complements in x, y, and z direction.

After sweep off of an RF pulse, spins will revert to their equilibrium position via transitions of protons from the higher energy level to the lower energy level. This transition is achieved by dissipating the excess energy as heat to the surrounding environment (or lattice). The process, known as T_1 relaxation, corresponds to the total

magnetic moment realigning over time with the constant B_0 leads to a gradual increase in the longitudinal magnetization. Formally this process can be described

$$M_z(t) = M_z(0)e^{-t/T_1} + M_0(1-e^{-t/T_1}) \tag{5}$$

where M_0 is the equilibrium magnetization parallel with B_0 before an RF pulse is applied. M_z is the z component of the total magnetization at time t.

Each proton produces a small magnetic field at its close neighbor and interacts with each other. Thus the static filed B_0 is spread over. Therefore, individual protons will lose phase with each other causing a decrease in transverse magnetization due to different frequencies. As mentioned before, the characteristic time for this dephasing the spin system is known as T_2. However, in practices, there is an additional dephasing factor introduced by external field inhomogeneities. Therefore, the overall observed or effective spin-spin relaxation time T_2^* characterizes dephasing due to both B_0 inhomogeneity and transverse relaxation. Formally the T_2^* processes can be described by

$$M_\perp(t) = M_\perp(0)e^{-t/T_2^*} \tag{6}$$

$$\frac{1}{T_2^*} = \frac{1}{T_2} + \frac{1}{T_2'} \tag{7}$$

where $M_\perp(0)$ is the initial amount of transverse magnetization immediately following an RF pulse. Let $M_\perp(t)$ is the amount of transverse magnetization at time t.

Figure 9 shows how the signal from a spin echo sequence decays over time. A line drawn through the peak amplitude of a large number of spin echoes describes the T2 decay, while individual spin echoes exhibit T_2^* decay.

Signal strength decays with time to varying degrees depending on the different materials in the sample. Different organs have different T_1s and T_2s and hence different rates of decay of signal. When imaging anatomy, some degree of control of the contrast of different organs or parts of organs is possible by varying TR and TE. Figure 5 shows pictorially how these two relaxation works.

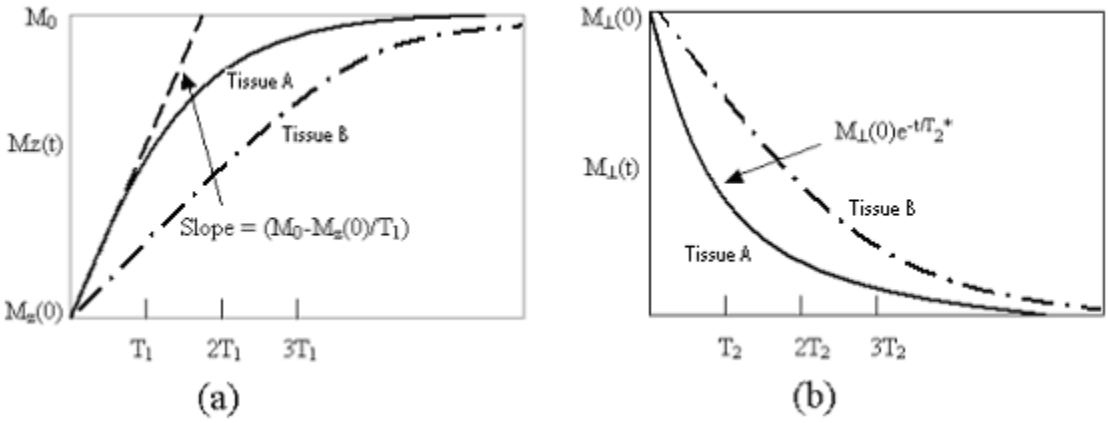

Figure 5: (a) The recovery of the T_1 relaxation from the initial value $M_Z(0)$ to the equilibrium value M_0. (b) T2* decay of signal with time

2.4 Image Formation

In order to convert the resonance into 2D or 3D distributions within the sample from which the RF signal was emitted, one can subject the sample a superimposing gradients magnetic field – a field which whose strength varies spatially. According to the

Larmor equation, the magnetic field gradient causes identical nuclei to precess at different Larmor frequencies. In this case, the sample which is located where the strength of field is smaller will resonance at a lower frequency relative to the sample in a stronger magnetic field. Thus, from the different resonance frequencies, we can obtain spatial information of the sample. There are three different uses of gradient fields.

A slice-selective excitation is to isolate a single plane in the sample being imaged, by only exciting the spins in that plane. First, a gradient filed is applied in the B_0 direction such that the Larmor frequency of the spins is dependent on their position along the z-axis. Then a shaped RF pulse applied will excite only a narrow plane perpendicular to the applied gradient. Everywhere else in the sample is receiving the wrong frequency of excitation for resonance to occur. This technique allows a slice, with thickness determined by the magnetic field gradient strength and the RF pulse bandwidth, to be selected from a sample.

A phase-encoding is a gradient field applied in the y-direction, which is orthogonal to both the slice selection gradient and the frequency-encoding. The phase encoding gradient does not change the frequency of the received signal because it is not on during signal acquisition. It serves as a phase memory, remembering relative phase throughout the slice. When turning on the phase-encoding gradient, each spin in the y-direction will have its own unique Larmor frequency. The phase of the precessing spins is then a function of location along the y-direction.

A frequency-encoding gradient is a gradient field applied in the x-direction. Then spins will precess at rates dependent on their x-direction location when the frequency-

encoding gradient is turned on. The frequency-encoding gradient is turned on just before the receiver is gated on and is left on while the signal is sampled or read out. For this reason the frequency encoding gradient is also known as the readout gradient.

In summary, three magnetic field gradients, placed orthogonally to one another inside the bore of the magnet, are required to encode information in three dimensions. After the slice-selective excitation a phase-encoding gradient is applied. Once the phase-encoding gradient pulse is turned off a frequency encoding gradient pulse is turned on. Then each of spin in the slice will have a unique phase angle and precessional frequency Subsequently, we encode each spin position in three dimensions.

2.5 MRI Sequences

There are many parameters can affect MRI signal intensity during MRI data acquisition, including, for instance, proton density, repetition time (TR) and echo time (TE). By choosing proper combination of pulse sequence parameters, one can generate different contrast among soft tissue, which can be beneficial for different pathologies. TR is the time between two consecutive RF pulses. For a given type of nucleus in a given environment, TR determines the amount of T_1 relaxation. The longer the TR, the more the longitudinal magnetization is recovered. Tissues with short T_1 have greater signal intensity than tissues with a longer T_1 at a given TR. TE is defined as the time between the start of the RF pulse and the maximum in the MRI signal. TE determines how much decay of the transverse magnetization is allowed to occur before the signal is read. It therefore controls the amount of T_2 relaxation. The application of RF pulses at different

TR values and the receiving of signals at different TE values produce variation in contrast in MR images. Here we describe two basic MRI sequences.

The spin echo (SE) sequence is the most commonly used pulse sequence in clinical imaging. It uses 90° RF pulses to excite the magnetization and 180° pulses to refocus the spins at TE to generate signal echoes (see Figure 6). The pulse sequence timing (TE and TR) can be adjusted to give T_1-weighted, proton or spin density, and T_2-weighted image contrasts. In T_1-weighted images, tissues that have short T_1 relaxation times (such as fat) present as bright signal. Tissues with long T_1 relaxation times (such as cysts, cerebrospinal fluid and edema) show as dark signal. In T_2-weighted images, tissues that have long T_2 relaxation times (such as fluids) appear bright. Proton density-weighted images also allow distinction of white and gray matter, with tissue signal intensities mirroring those obtained on T_2-weighted images. In general, T_1-weighted images provide excellent anatomic detail, while T_2-weighted images are often superior for detecting pathology.

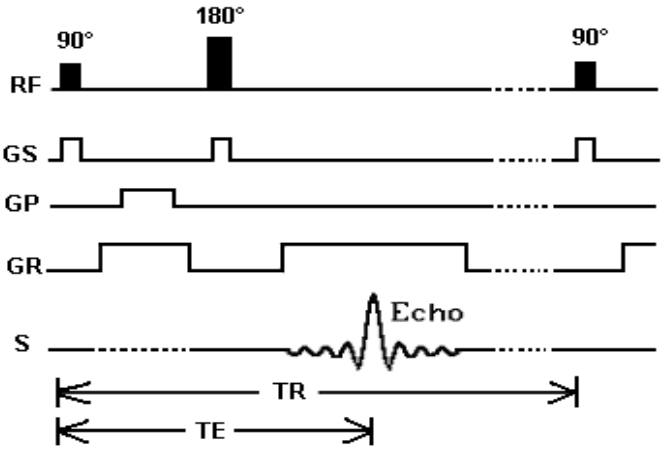

Figure 6: A simple spin-echo sequence timing diagram.

Gradient echo (GRE) sequences, which show a wide range of variations compared to the spin echo, are significantly faster than SE sequences. GRE sequences differ from SE sequences in that there is no 180° refocusing RF pulse (see Figure 7). In addition, the flip angle is usually at or close to 90° for a spin echo sequence but commonly varies over a range of about 10° to 80° with gradient echo sequences. With a shorter TR, GRE sequences have less scan time, but this is at the expense of the signal to noise ratio (SNR). At the interface of bone and tissue or air and tissue, there is an apparent loss of signal that is heightened as TE is increased. Therefore it is usually inappropriate to acquire T_2-weighted images with GRE sequences. Nevertheless, GRE sequences are widely used for obtaining T_1-weighted images for a large number of slices or a volume of tissue in order to keep scanning times to a minimum. GRE sequences are often used to acquire T_1-weighted 3D volume data that can be reformatted to display image sections in any plane. However, the reformatted data will not have the same in-plane resolution as the original images unless the voxel dimensions are the same in all three dimensions.

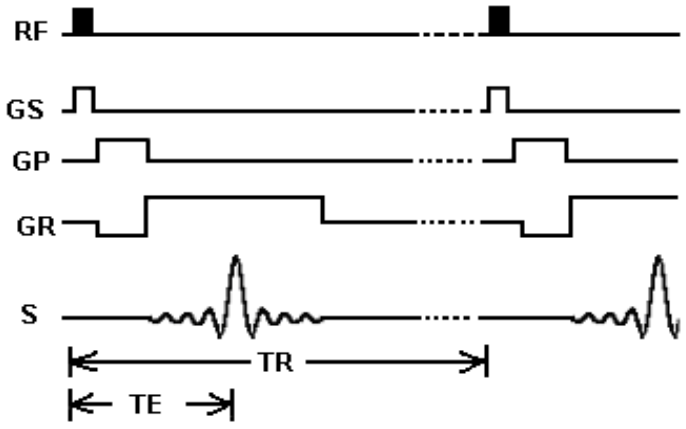

Figure 7: A simple gradient-echo sequence timing diagram.

3. THEORY AND METHOD

3.1 FLASH Imaging Theory

The Fast Low-Angle Shot sequence (FLASH) is a gradient echo sequence that utilizes a spoiler gradient on the slice select axis during the end module (Figure 8) to destroy any remaining x-y (transverse) magnetization after the readout module, which is the case for short repetition times. As a result, only z-magnetization remains during a subsequent excitation.

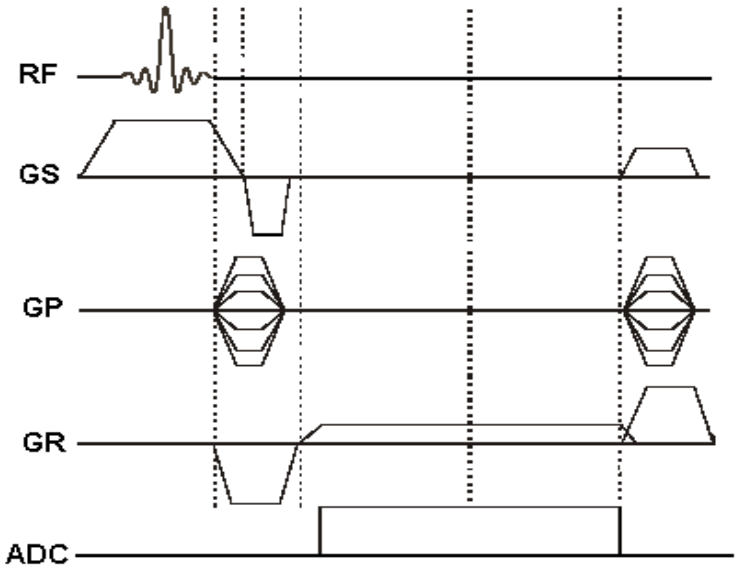

Figure 8: FLASH sequence timing diagram

The signal intensity of a FLASH sequence is given by

$$S \propto \rho M_0 e^{-TE/T_2^*} \frac{1 - e^{-TR/T_1}}{1 - \cos(\alpha) e^{-TR/T_1}} \sin(\alpha) \tag{8}$$

where ρ is the proton density, M_0 the main magnetization. Since the TE determines the degree of T_2^* in the FLASH image and sensitivity to motion, it is typically preferred that TE is as short as possible. Note that for TE $<<$ T_2* and large, the above expression yields relatively high signal and becomes independent of T_2*, hence the term T_1-weighting. Assuming adequate spoiling and ignoring T_2* effects and receiver sensitivity, the signal intensity (S) dependence on flip angle (α) and T_1 of a FLASH image [16] in Eq. (8) can be simplified as

$$S \propto \rho M_0 \frac{1 - e^{-TR/T_1}}{1 - \cos(\alpha) e^{-TR/T_1}} \sin(\alpha) \tag{9}$$

In the literature, Eq. (9) is usually used to describe the image intensity of a FLASH image. However, Eq. (9) doesn't consider the reception sensitivity factor of the coil when the same coil that is used for excitation is also used for reception. Therefore, we think the signal expression for the image needs to be modified to include the reception sensitivity of the coil. Assuming that the principle of reciprocity applies [23], the signal expression of a FLASH image is determined by,

$$S \propto \rho M_0 \kappa \frac{1 - e^{-TR/T_1}}{1 - \cos(\kappa \cdot \alpha) e^{-TR/T_1}} \sin(\kappa \cdot \alpha) \tag{10}$$

where κ is a spatially dependent sensitivity factor which modulates both the excitation flip angle and the reception sensitivity, and α is the nominal flip angle. Note that the

effective flip angle is scaled with κ now. Since the signal in Eq. (9) decreases with the flip angle for angles above the Ernst angle, and the receiver sensitivity that is proportional to B_1 generated by the coil depends on κ linearly, it is anticipated intuitively that the measured signal, described by Eq. (10), may have an approximately constant value over a range of κ for which the flip angle is above the Ernst angle. This approximately constant signal regime can then be used for obtaining uniform FLASH images.

To verify the above conjecture, numerical calculations in Matlab 6.0 (Mathwork Inc.), using Eq. (10), of measured FLASH signal intensities of white matter (WM) and gray matter (GM) as a function of κ values were performed for various nominal flip angles (assuming M_0 is equal to 1 in this case). Here T_1 values of 788 msec and 1286 msec were used for WM and GM respectively for magnetic filed strength at 3 Tesla [24]. Normalized proton densities [25] for WM (0.61) and GM (0.69) were also included in the calculation. The estimated the Ernst angle were calculated by

$$\theta = \cos^{-1}(e^{-TR/T_1}) \tag{11}$$

For the above parameters, the Ernst angles were 15º and 19º for GM and WM respectively. The result for α = 15°, 45º and TR of 45 msec (a typical value for 3 D anatomic brain imaging) were shown in Figure 9. Figure 9 clearly demonstrates that the observed signal intensity has a flat region over a range of κ when flip angle is greater than the Ernst angle. Because the nominal angle is above the estimated Ernst angle the flat range is around κ=1. For most imaging setups, the nominal flip angle which is setup

in the FLASH pulse sequences is the average of the actual measured flip angle. Therefore, actual measured flip angles over the Field of View (FOV) center on the nominal angle and κ fluctuates about 1. As a result, it is important for the region around κ of 1 to be as flat as possible to achieve uniform intensity within the same tissue in the acquired image.

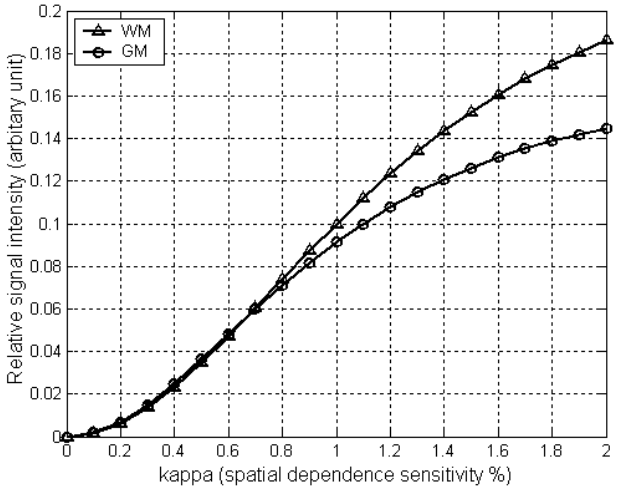

(a)

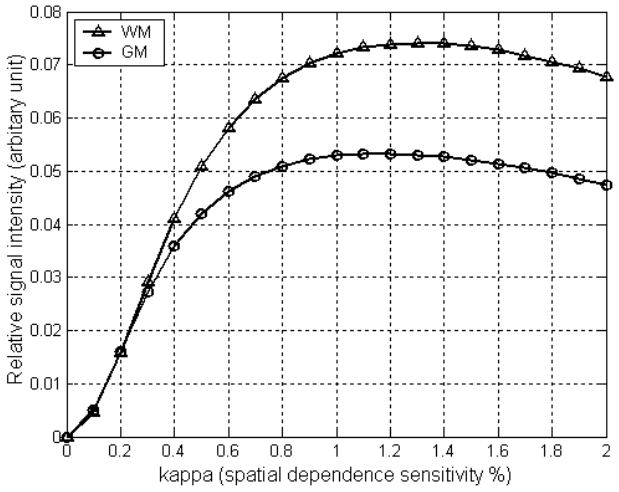

(b)

Figure 9: Simulated FLASH image signal intensity versus κ (spatially dependence sensitivity factor) at a nominal flip angle of 15º (a) and 45º (b) in WM (T_1 = 788 ms, ρ_0 = 0.61) and GM (T_1 = 1286 ms, ρ_0 = 0.69) at 3T.

Based on Eq. (10), it is expected that for small nominal flip angle (< or ~ Ernst angle), the flat region will not appear around κ of 1 and therefore the acquired image will not have uniform intensity for the same tissue. This is numerically demonstrated in Figure 10 where Eq. (10) was evaluated around κ of 1 for the nominal flip angles of 20º, 40º, 60º, and 80º, respectively. To demonstrate the relative intensity changes among different nominal flip angles, the intensities in Figure 10 were normalized by the white matter intensity at κ=1 and nominal flip angle of 20º. Normalized proton-densities for the white matter and gray matter were also taken into account in deriving the intensities in Figure 10.

As can be seen in Figure 10, the signal intensities of WM and GM are not flat around κ of 1 for the flip angle of 20º. In contrast, when the nominal flip angle is much larger than the Ernst angle, for instance, $\alpha = 60º$, the simulated signal intensity is virtually constant and approximates a leveled line. This simulation indicates that, when a sufficiently large flip angle is used, the image intensity within the same tissue will be uniform. It is also interesting to note that the signal intensity difference between the gray and white matter, which is defined as the image contrast, remains approximately constant for a large range of κ for nominal flip angles greater than the Ernst angle.

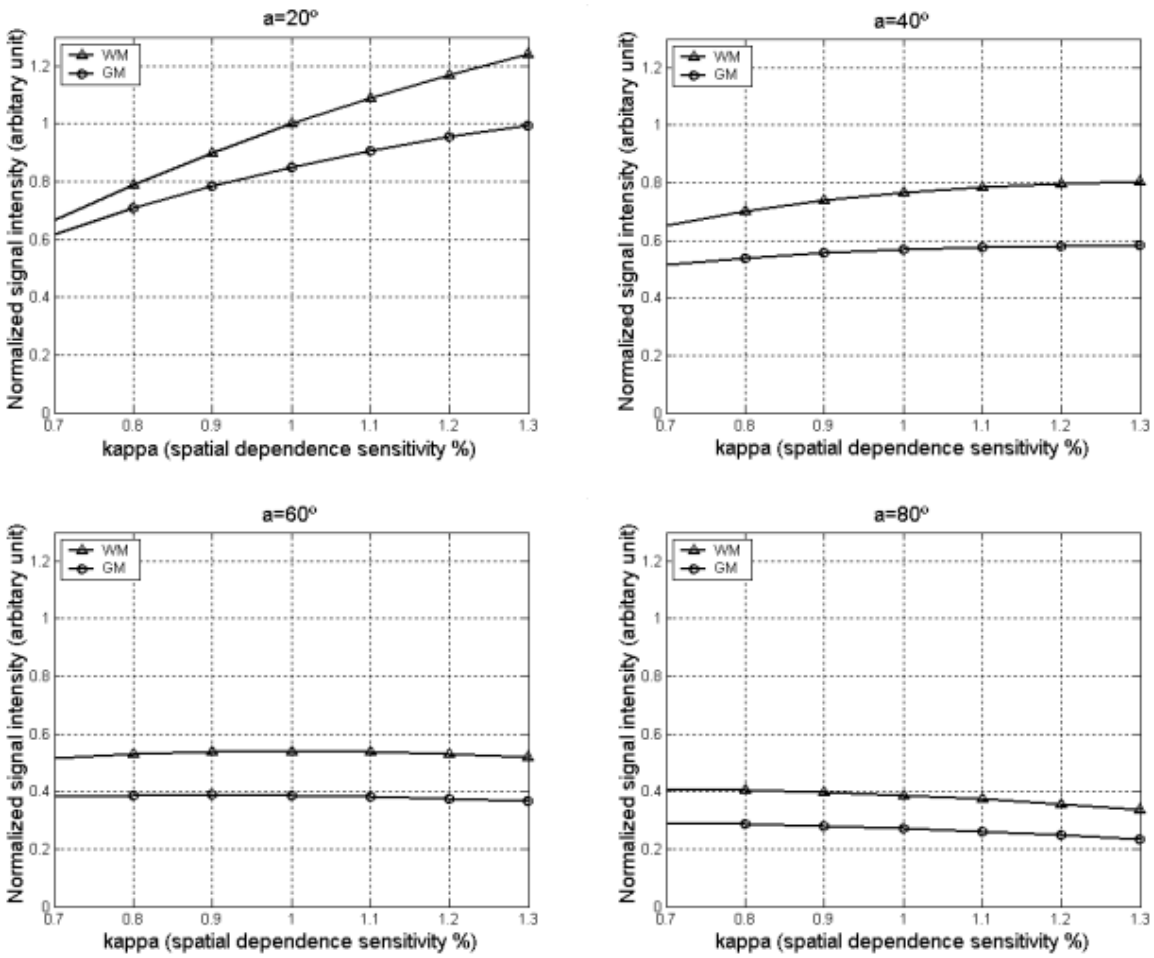

Figure 10: Simulated FLASH image signal intensity changes with κ in the range of 0.7 to 1.3 for TR=45 ms in GM (T_1 = 1286 ms, ρ_0 = 0.69) and WM (T_1 = 788 ms, ρ_0 = 0.61) at 3T. The intensities were normalized by the white matter intensity at κ=1 and nominal flip angle is 20°. The signal intensity changes very slowly when the flip angle is at 60º.

3.2 Method

To confirm the above numerical prediction, experimental work was conducted as followings. A Siemens 3 Tesla Trio™ whole-body MRI scanner system equipped with a Sonata gradient set capable of 40 mT/m with a maximum rise time of 200 μs was used

for this study. A Siemens OEM head coil was used for data acquisition. Since imperfect slice profiles associated with selective excitation pulses may introduce a modulation of α across the slice, complicating Eq. (10), a non-selective excitation pulse was used in conjunction with a 3D-FLASH sequence for simplicity. Experimental data were first collected on a spherical phantom ($T_1 \approx 1240$ msec at 3T) using a TR of 45 msec, a TE of 2.61 msec, an FOV of 238mm×208mm×202mm, a matrix of 128×112×96, and nominal flip angles of 10º, 20º, 30º, 40º, 50º, 60º, 70º and 80º, respectively. In addition to the phantom experiment, an *in vivo* study was also performed on 3 healthy male volunteers with approved IRB protocol to verify the validity of our theoretical prediction *in vivo*. In this case, the 3D-FLASH sequence parameters consisted of a TR of 45 msec, a TE of 2.70 msec, an FOV of 200mm×200mm×166mm, a matrix of 128×128×104, and nominal flip angles of 15º, 30º, 45º, 60º, 75º and 85º, respectively.

The resultant data were processed using routines implemented in IDL (Research Systems Inc.). A 3D image data set was created for each flip angle. In order to make a simple quantitative comparison of the dependence on flip angle, a single slice in the axial direction (z-direction) from the 3D data set was analyzed. For phantom images, slice No. 64 (in the axial direction) was used in the analysis. A profile of the image (along the line indicated in Figure 11) was also examined. In addition, several region of interests (ROI) at the edge and center of phantom image number 64 (black circles in Figure 11) was created and used to calculate the range of intensity over the phantom for each nominal flip angle. These analyses were similarly performed on the human data set. For the human data, an axial slice number 64 was analyzed. Profiles of the image along a line

(indicated in Figure 14) that resided in the white matter were quantitatively analyzed for each angle. Because the profile from the human images was fairly noisy, the profiles were fitted to a second-order polynomial curve before the intensity range of the fitted profiles were calculated to ascertain the spatial variation. In addition, the human subject images also were segmented based on signal intensity for different nominal flip angles. The areas of WM and GM in each segmented image were calculated to quantitatively analyze the effect of flip angles on the image inhomogeneity.

4. RESULTS AND DISCUSSION

4.1Phantom results

As previously mentioned, when a perfect the head coil without RF nonuniformities was employed on a uniform sample, the acquired sample images would exhibit a constant gray level and could be determined by a spectral calibration. In order to enable to see the effects of the RF informality at different flip angles, it is desirable to scan a uniform sample. In Figure 11, images of the uniform phantom (filled with 8.2g CH_3COONa and 9.6g $C_3H_5LiO_3$ and 1000g H_2O diameter: 10cm, 96.14% water) acquired at four different flip angles 20º, 30°, 40° and 50º, respectively, are shown. It is easy to see that spatial variation in the image obtained with 10° (< Ernst angle) and 20º (~Ernst angle) flip angles is severe. As shown in Figure 11, the center of the image with a flip angle of 10° or 20º is much brighter than the surrounding areas in that image. Comparing to the image with a flip angle of 10° or 20º, the uniformity of signal intensity in the image with a flip angle of 40° or 50º is significant improved.

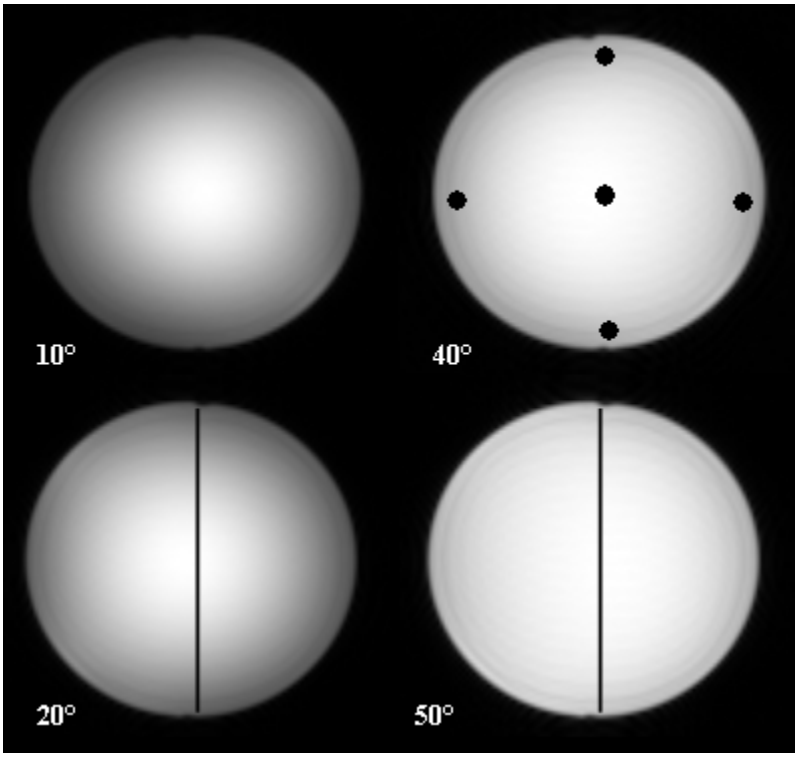

Figure 11: Phantom image with a flip angle of 10°, 20°, 40° and 50º. The black lines in the bottom two images are profile location. The black circles in right-up concern are ROI selected for intensity calculation

This dependence of image uniformity on the nominal flip angle can also be observed in the profiles of images obtained at different flip angles. For demonstration purposes, only vertical profiles from images with a flip angle of 20° and 50º are shown in Figure 12, where the profile of 50º (solid line) is approximately flat while that of 20º (dash line) exhibits substantial variation.

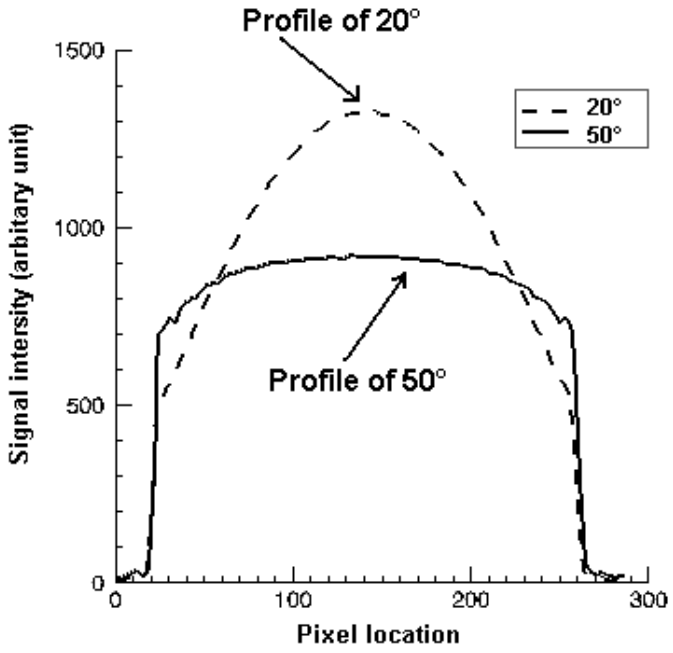

Figure 12: Phantom image vertical cross-over profiles for flip angle α=20° (close to Ernst angle) and 50°

In order to make a quantitative comparison of the effect of flip angle on the image homogeneities and reduce the noise contamination in the image, the normalized phantom image intensity range for the ROIs (shown in Figure 11), which include four edge ROIs and one center ROI in the image, were calculated by

$$Normalized\_range = \frac{mean(ROI\_center) - mean(ROI\_edge)}{mean(ROI\_center)} \tag{12}$$

where *ROI_center* and *ROI_edge* represent the measured signal intensity for the ROI located at center and edge of the image. The results of the normalized intensity for the phantom data at different nominal flip angles are listed as follows:

Table 1: Measured phantom data signal intensity range at different nominal flip angle

	10°	20°	30°	40°	50°	60°	70°	80°
Mean(ROI_center)	937.85	1326.5	1283.4	1092.9	914.30	784.48	685.20	593.19
Mean(ROI_edge)	338.07	586.21	715.10	745.08	716.67	658.83	590.79	531.03
Normalized range	0.6395	0.5581	0.4428	0.3183	0.2162	0.1602	0.1378	0.1048

Be reviewing Table 1, it was found the normalized intensity range results in the phantom image decreases with α. That means the signal intensity uniformity in measured ROIs was improved at the higher nominal flip angle. In order to tell the difference easily, the normalized intensity range of the phantom image is plotted against the nominal flip angle in Figure 13. As Figure 13 indicates, the normalized phantom image intensity range with nominal flip 20° is equal to 0.558. In contrast, when a 50º nominal flip angle was used, the variation decreased to a negligible level (such as in Figure 12) and the normalized intensity range dropped to 0.216, approximately one third of that at 20º.

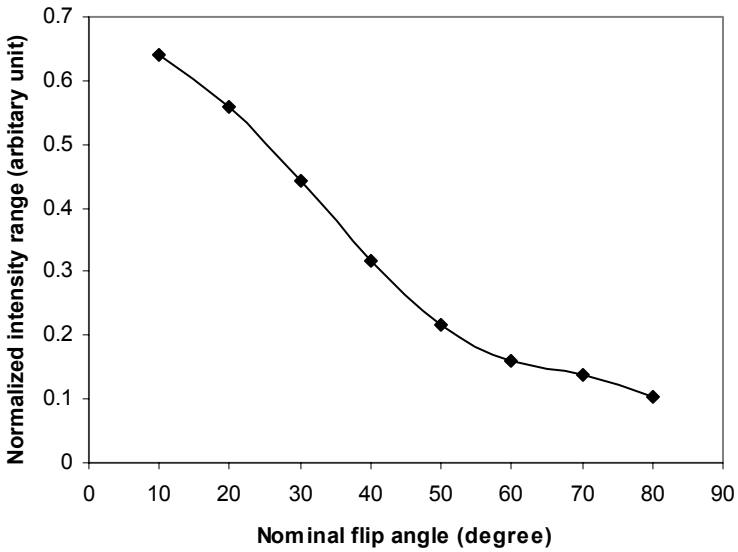

Figure 13: The normalized phantom image intensity range decrease with the increase of the nominal flip angle.

Up to this point, the effects of the nominal flip angles on the FLASH phantom data had been based on the image profile and normalized intensity ranges. As previously mentioned, it was found that both image profiles and normalized intensity ranges were enhanced when the lager nominal flip angles were applied. Although the signal intensities were degraded for larger flip angles, this result, in agreement with the theoretical analysis given above, suggests that a nominal angle between 40º- 60º would result in the best image uniformity for this situation when considering the SNR reduction at larger flip angles.

4.2 Normal human volunteer results

Like the phantom study, an *in vivo* experiment was also conducted with normal healthy male volunteers. For demonstration purpose, only one slice in the transverse direction (z-direction) from each constructed 3D data set at different nominal flip angles was selected. The results are illustrated in Figure 14. As shown in Figure 14, similar to the previous phantom data results, the image of the smallest flip angle used, 15º in this case, exhibits the largest spatial variation, brighter in the center than the outer regions. In contrast, this spatial variation is diminished in the image with larger nominal flip angle, for instance, 45° or 60°. Beyond the above intensity variation, it was found another difference among the human brain images was the appeared contrast. Images that used lower flip angle had poor WM and GM contrast compared to those that used the higher flip angle. However, the contrast difference among those higher flip angle images was relatively small.

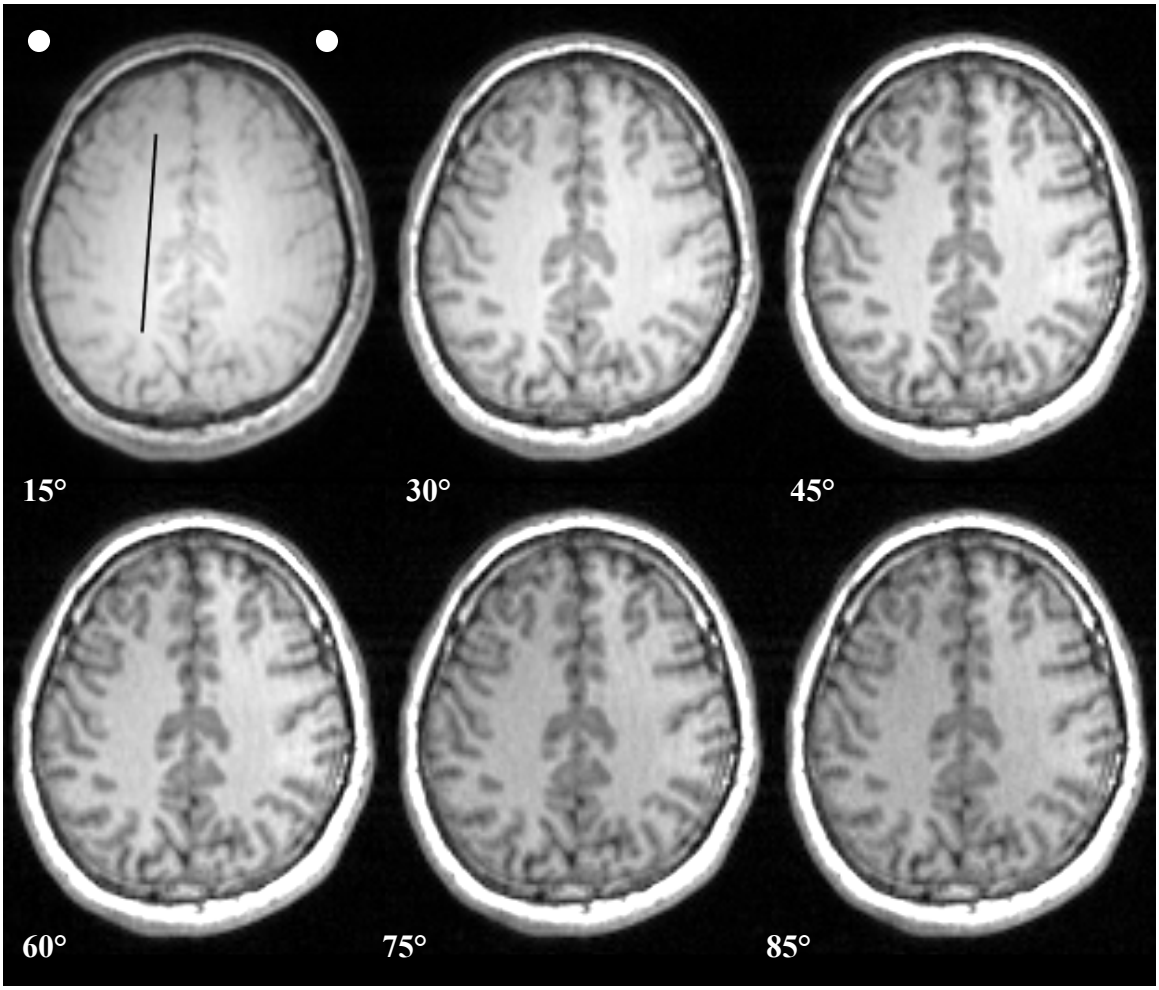

Figure 14: Normal human subject brain images (axle direction) at different nominal flip angles. The two white circles are background ROIs used for noise analysis.

To evaluate the image uniformity, it is necessary to examine signal within the same tissue. Thus, a line within the white matter, as indicated in Figure 14, was defined for profile analysis. As phantom profiles shown in Figure 12, the signal intensities profile of brain image with flip angles at 15º and 45º were plotted in Figure 15. Comparing to the

profile of 15º (solid line) which exhibits substantial variation, the profile of 45º (dash line) is almost flat.

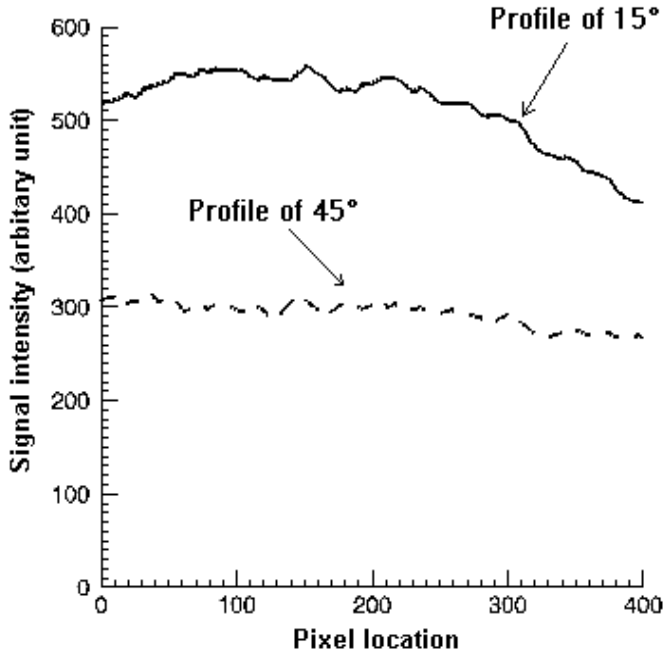

Figure 15: Human brain image vertical profiles in the white mater with the nominal flip angle α=15° and 45°.

Because the human images themselves are noisier than the uniform phantom images, to avoid the effect of noise on the quantitative analysis, curve fitting is necessary. In this case, each profile that is sitting in the WM at different flip angle was fitted to a second-order polynomial curve and the resultant fits were used for intensity variation analysis. In addition, since each image has different signal intensity level due to different nominal flip angle, to make a quantitative comparison, the normalized brain image intensity range was calculated from each fitted profile by

$$Normalized\_range = \frac{\max(fitted\_pro) - \min(fitted\_pro)}{\max(fitted\_pro)} \quad (13)$$

where *Max(fitted_pro)* and *min(fitted_pro)* represent the maximum and minimum signal intensity of the second-order polynomial fitted profile. The results of the normalized intensity for the phantom data at different nominal flip angles are listed as follows:

Table 2: Measured brain image profile signal intensity range at different nominal flip angle

	15°	30°	45°	60°	75°	85°
max(fitted_pro)	550.77	434.42	305.560	220.78	161.63	136.93
min(fitted_pro)	406.56	358.13	265.61	195.37	147.44	125.28
Normalized range	0.2618	0.1756	0.1307	0.1151	0.08780	0.0851

As shown in Table 2, it was found the normalized intensity range in the brain image decreases with α. That means the signal intensity is more uniform for the curve fitted profile at the higher nominal flip angle. To tell the difference easily, the normalized intensity range of the brain image is plotted against the nominal flip angle in Figure 16. For example, as Figure 16 indicates, the normalized phantom image intensity range with nominal flip 15° (~Ernst angle) is equal to 0.2618. In contrast, when a 45º nominal flip angle was used, the normalized intensity range dropped to 0.1307, approximately one half of that at 15º.

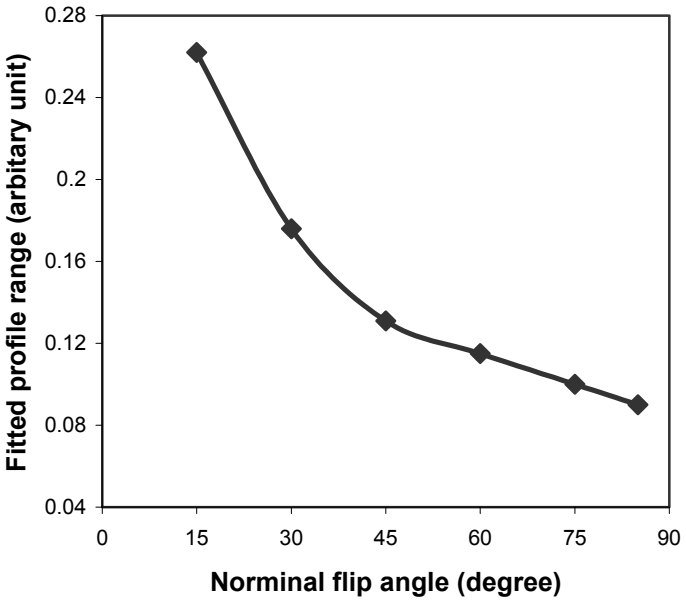

Figure 16: The normalized human brain image intensity range decrease with the increase of the nominal flip angle.

This result exhibits good correspondence with the phantom results in Figure 13. At a nominal flip angle of 15º, the normalized signal intensity range is much larger than that at other angles. When the flip angle increased to 45º, 60º, and 75º, the normalized intensity ranges dropped to less than half of that of 15º. A broad shoulder with a gradual decrease is seen between 40º and 75º. This result qualitatively parallels the phantom result and demonstrates that insensitivity to RF inhomogeneity can be achieved if a sufficiently large flip angle is used during the data acquisition. Of course, the exact angle at which this insensitivity is optimal depends on the TR, the T_1 of the tissue of interest and the spatial distribution of the RF field.

4.3 Image segmentation test

Segmentation of MR images into different tissue classes, especially gray matter, white matter and cerebrospinal fluid (CSF), is an important task for many medical applications such as identifying anatomical region of interest (ROI) for diagnosis and treatment or localizing anatomical ROI functional correlation. Such tissue segmentation is often achieved by applying statistical methods, in conjunction with mathematical morphological image processing operations [26], to label pixels according to the intensity values. However, if the same tissue in the images were not uniform due to B_1 inhomogeneity, the segmentation results would be disturbed. In the ideal case, differentiation between white and gray matter in the brain should be easy since these tissue types exhibit distinct signal intensities. In practice, spatial intensity inhomogeneities are often of sufficient magnitude to cause the distributions of signal intensities associated with these tissue classes to overlap significantly. Therefore, by applying intensity based image segmentation, the effect of inhomogeneities at different nominal flip angles on the FLASH image can be tested. In this thesis, FSL (written mainly by members of the Image Analysis Group, FMRIB, Oxford, UK) [27], which applied advanced techniques such as non-parametric, multi-channel methods, was used for this purpose. The same images slice from each segmented results using FSL are selected and are shown in Figure 17:

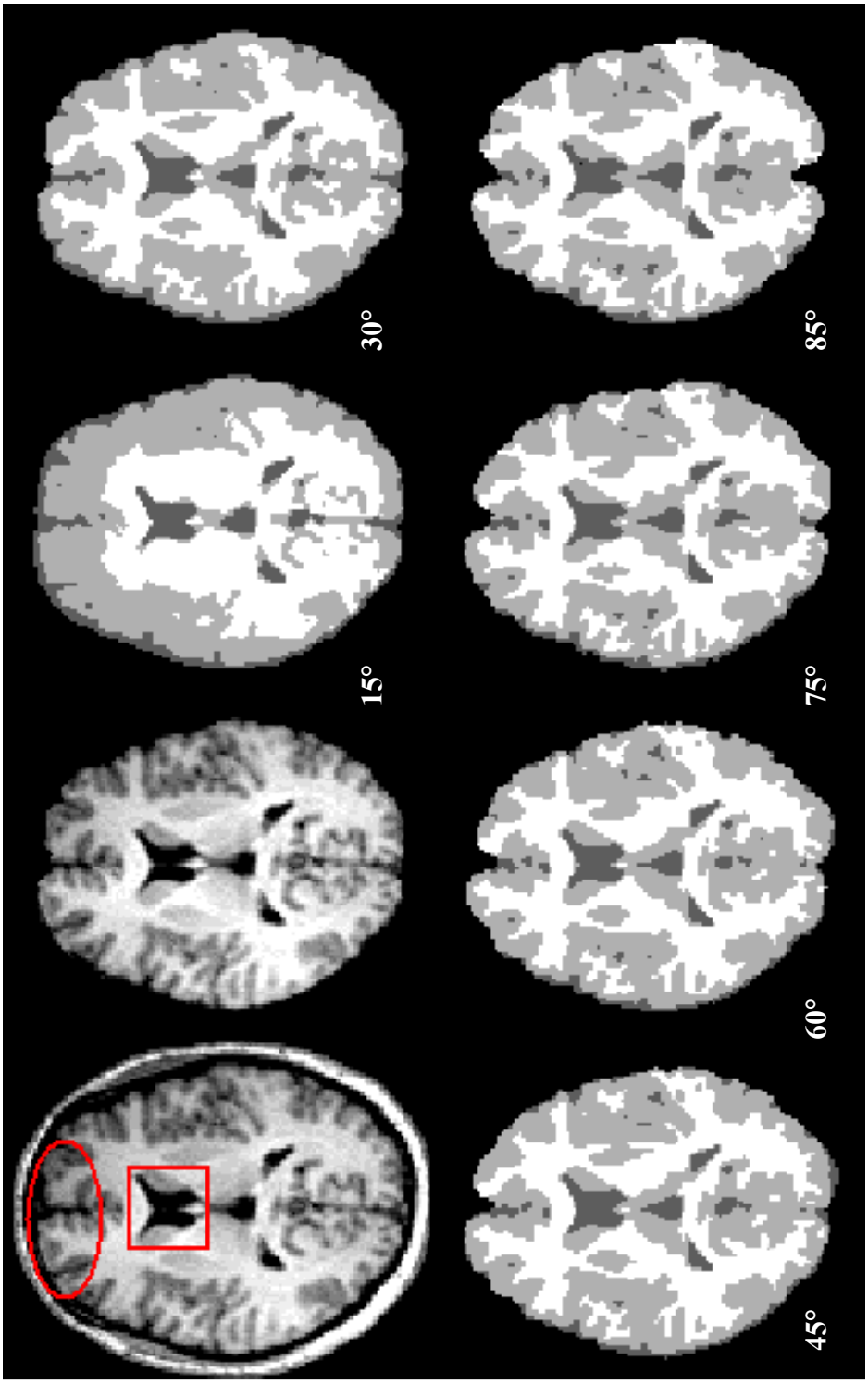

Figure 17: The effect of different flip angles on the FLASH image segmentation

Figure 17 clearly indicates that the disturbance of the classification for segmentation at α=15°. In this segmentation the white matter is completely absent in the frontal brain tissue. Note the significant improvement for segmentation when larger flip angle was used. In addition, Notice that the anterior horn of the lateral ventricle at the center of the original image (highlighted by the small rectangle in Figure 17) where there is less B_1 inhomogeneity effect, looks fairly identical in all segmented images. However, when comparing the WM located at the outer of the original image (highlighted by circle in Figure 17) where there is larger B_1 inhomogeneity effect, the relative large variations are noticeable among the segmented image at different flip angles. It was apparent that the segmented images using low flip angle was less accurate than those images using high flip angles. This indicated the segmentation performance for higher flip angle is better. In other words, the FLASH image using a higher flip angle is seen to be more uniform from the segmentation point of view. In order to compare the difference among the segmented images at various flip angles, the percentages of WM and GM areas were calculated by dividing the number of differently labeled pixels image by the total number of pixels within the segmented image. The percentages of difference between WM and GW were also calculated. The results are graphically shown in Figure 18:

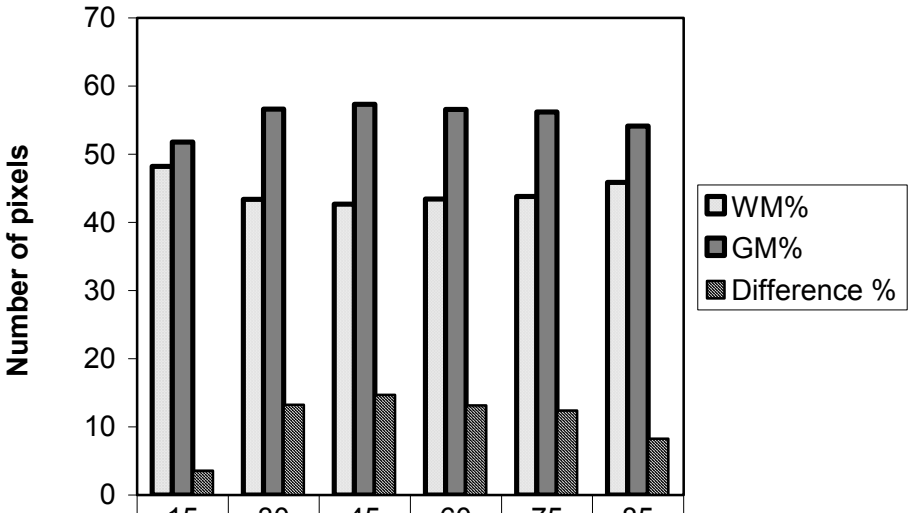

	15	30	45	60	75	85
WM%	48.22	43.39	42.66	43.42	43.79	45.86
GM%	51.78	56.61	57.34	56.58	56.21	54.14
Difference %	3.562	13.22	14.69	13.16	12.42	8.273

Nominal flip angle (degree)

Figure 18: The percentage difference of WM and GM in the segmented image.

As shown in Figure 18, it was found that the percentages of WM and GM were 48.22% and 51.78 % in segmented image for flip angle at 15°, which is abnormally higher (WM%) and lower (GM%) than the results from other flip angles. In contrast, when the larger flap angles were used, the percentages of WM and GM were kept very small variations around 43% and 56% among the higher flip angles. The segmentation results were stabilized at higher flip angles. This indicated the contrasts of image are well reserved when the high flip angles are applied in the FLASH imaging.

4.4 Image contrast vs. intensity

Since noise is common in MRI images, in order to compare the effect of flip angle on image homogeneity, it is desirable to analyze the signal-to-noise ratio (SNR) and contrast-to-noise ratio (CNR). In this case, assuming the background noise is constant and it is the same for all FLASH images, the estimated the image noise [28] can be calculated by

$$\sigma_{background} = \sigma_{image}\sqrt{\frac{\pi}{2}} \approx 1.25\sigma_{image} \tag{14}$$

where σ_{image} and $\sigma_{background}$ are the standard deviation of image and background. To simplify the noise measurement, two small ROIs at corner of image (see Figure 14) were used for background noise calculations. The results for WM and GM intensities and measured background noise are list in Table 3

Table 3: Signal intensity of WM and GM and measured the background noise.

	15°	30°	45°	60°	75°	85°
White Matter	492.54	443.94	336.25	248.18	188.72	158.40
Gray Matter	417.91	319.31	226.40	161.46	122.64	105.58
Contrast (WM-GM)	74.63	124.63	109.85	86.72	66.08	52.82
Background noise	4.26	4.36	4.21	4.27	4.09	4.07

This result also was shown in Figure 19 where both measured data and simulation data were normalized to the same scale. In Figure 19, we present data demonstrating the

dependence of signal (or signal-to-noise ratio as noise is constant) and contrast on the flip angle. Specifically, the measured signal in white matter (gray matter signal shows similar trend but not included to avoid cluttering the figure) is plotted versus flip angle and compared with numerical calculations (assuming TR = 45 ms, GM T_1 = 1286 ms, WM T_1 = 788 ms, and κ = 1.10).

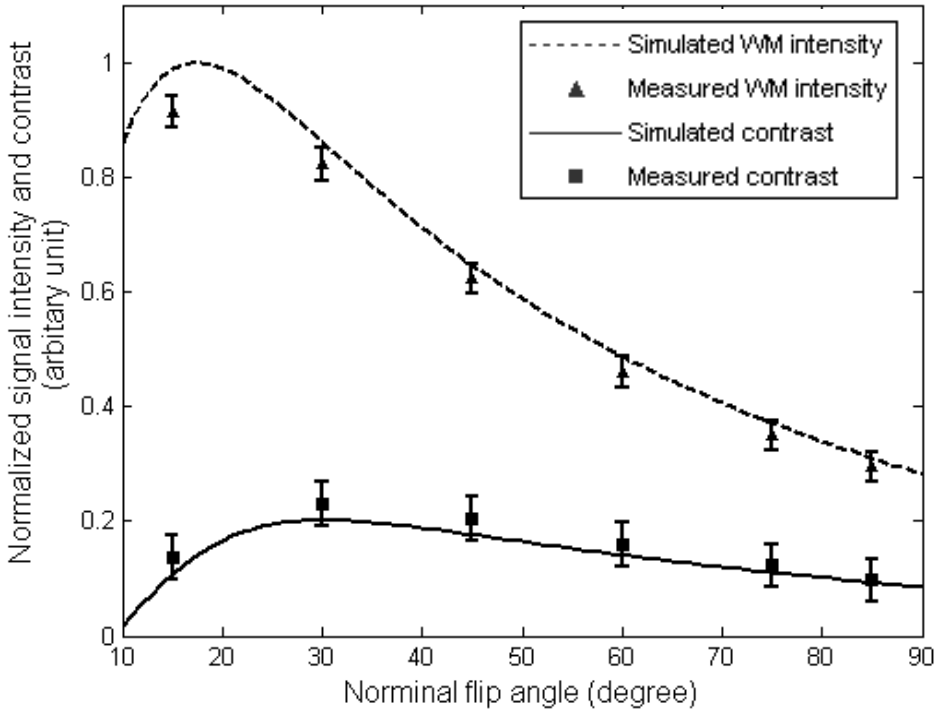

Figure 19: Comparing normalized contrasts, WM intensity simulation with measured contrasts and intensity at various flip angles. The simulated contrast was fitted with κ of 1.10.

Undoubtedly, there is a significant signal (and SNR) reduction with increasing flip angles because the angles used were mostly above the Ernst angle. While the overall SNR is an important image quality measure, a more important measure is the contrast (or

equivalently contrast-to-noise as noise level remains the same). Thus Figure 19 also provides a comparison of the numerically derived WM vs. GM contrast as a function of flip angle with the experimentally obtained values. A good agreement between the simulation and the experiment is a strong evidence to verify the previous theory that the higher flip angle can improve the B_1 homogeneity in FLASH images. Although all TR, TE and flip angle can be manipulated in FLASH imaging, TR itself has little effect on contrast as long as the RF pulse is properly chosen (longer TRs will result in higher signal to noise but with longer scan time). The flip angle has the largest effect on contrast. As TR is decreased the optimal flip angle becomes smaller. Smaller flip angles will produce predominately Proton Density weighted images. Larger flip angles produce more T_1-weighting. Although the contrast is also reduced a little at large flip angles, the contrast peaks at an angle larger than the Ernst angle (30º vs. 15º) and decreases slowly for large flip angles ($\alpha \geq 30º$). Since going beyond 60º only leads to a small improvement in uniformity (see Figure 15) but a substantial reduction in intensity, it is recommended that a flip angle between 40º-55º be used when other imaging parameters are the same as used in this experiment.

4.4 The validity consideration

It should be noted that the validity of Eq. (10) depends on two things: the validity of Eq. (9) and the validity of reciprocity theory. The former relies on complete spoiling of the any remaining transverse magnetization after readout module and ignoring T_2* effects. This assumption might be debased due to the imperfect gradient system

performance. The latter can also be violated when high magnetic fields [17] is applied for FLASH image. This factor may be already present in our collected human data with magnetic field strength at 3 Telsa although it is not very severe. However, for higher magnetic fields, the validity of the results reported in this paper may be degraded further due to the above reason. In addition, the operating conditions, temperature changes, status of the MR equipment and many other factors will also frequently affect the observed intensities, causing notable inter-scan intensity inhomogeneities. Undoubtedly, the flat region demonstrated in Figure 9 and Figure 10 can only be of a finite extent. Therefore, the insensitivity of FLASH imaging to RF inhomogeneity is only valid for a limited range of variations, which arises in relatively uniform coils, and unlikely valid over the entire sensitivity range of a surface coil.

5. CONCLUSION

It is demonstrated based on theoretical arguments and experimental data that the FLASH sequence can be made insensitive to RF inhomogeneity if a single coil is used for both transmission and reception and if a proper nominal flip angle is used. Under this condition, variations due to receiver sensitivity can be offset by the variations due to transmitter nonuniformities. Consequently, the deleterious effect of RF inhomogeneity in the image data can be substantially eliminated. Although better RF coil design can improve B_1 homogeneity and sophisticated post image processing algorithms can mitigate the effects of B_1 inhomogeneity, the observation described here for FLASH imaging has shown a simple way to be able to compensate to some degree for minimizing the effects of B_1 inhomogeneity. The noteworthy enhancement of human subjects MR imaging segmentation results, which are very sensitive to the uniformity of the image intensities, also indicated that image uniformity is improved at high flip angle.. While the technique reported in this thesis might lead to degrade the SNR in some degree, it represents a significant improvement in image homogeneity as well as image contrast between various tissues. Therefore, the observation reported in this thesis should be beneficial for choosing sequence parameters for using FLASH in anatomic studies.

REFERENCES

[1] Z. H. Cho, J. P. Jones, and M. Singh, *Foundations of Medical Imaging*. New York: Wiley-Interscinece, 1993.

[2] C. M. Collins, S. Li, and M. B. Smith, "SAR and B1 field distributions in a heterogeneous human head model within a birdcage coil," *Magn Reson Med*, vol. 40, pp. 847-856, 1998.

[3] Q. X. Yang, S. Li, and M. B. Smith, "The effect of sample loading on the radio frequency magnetic field distribution in high field: contributions of dielectric resonance," presented at 12th Annual Meeting of the Society of Magnetic Resonance in Medicine, New York, 1993.

[4] S. R. Simmons, G. J. Arridge, Barker, and S. C. Williams, "Sources of intensity nonuniformity in spin echo images at 1.5 T," *Magn Reson Med*, vol. 32, pp. 121-128, 1994.

[5] K. O. Lim and A. Pfefferbaum, "Segmentation of MR brain images into cerebrospina fluid spaces, white and gray matter," *J Comput Assist Tomogr*, vol. 13, pp. 588-593, 1989.

[6] P. A. Narayana and A. Borthakur, "Effect of radio frequency inhomogeneity correction on the reproducibility of intra-cranial volumes using MR image data," *Magn Reson Med*, vol. 33, pp. 396-400, 1995.

[7] S. Li, C. M. Collins, B. J. Dardzinski, C. L. Chin, and M. B. Smith, "A method to create an optimum current distribution, and homogeneous B1 field for elliptical birdcage coils," *Magn Reson Med*, vol. 37, pp. 600-608, 1997.

[8] J. T. Vaughan, H. P. Hetherington, J. O. Otu, J. W. Pan, and G. M. Pohost, "High frequency volume coils for clinical NMR imaging and spectroscopy," *Magn Reson Med*, vol. 32, pp. 206-218, 1994.

[9] A. H. Andersen, Z. Zhang, M. J. Avison, and D.M.Gash, "Automated segmentation of multispectral brain MR images," *J Neurosci Methods*, vol. 122, pp. 13-23, 2002.

[10] S. Clare, M. Alecci, and P. Jezzard, "Compensating for B1 inhomogeneity using active transmit power modulation," *Magn Reson Imag*, vol. 19, pp. 1349-1352, 2001.

[11] L. Q. Zhou, Y. M. Zhu, C. Bergot, A. M. Laval-Jeantet, V. Bousson, J. D. Laredo, and M. Laval-Jeantet, "A method of radio-frequency inhomogeneity correction for brain tissue segmentation in MRI," *Comput Med Imag Graph*, vol. 25, pp. 379-389, 2001.

[12] A. Koivula, J. Alakuijala, and O. Tervonen, "Image feature based automatic correction of low-frequency spatial intensity variations in MR images," *Magn Reson Imag*, vol. 15, pp. 1167-1175, 1997.

[13] K. Ugurbil, M. Garwood, A. R. Rath, and M. R. Bendall, "Amplitude-modulated and frequency phase-modulated refocusing pulses that induce plane rotations even in the presence of inhomogeneous B1 Fields," *J Magn Reson*, vol. 78, pp. 472-497, 1988.

[14] S. L. Talagala and J. Gillen, "Experimental-determination of 3-Dimensional RF magnetic-field distribution of NMR coils," *J Magn Reson*, vol. 94, pp. 493-500, 1991.

[15] R. Deichmann, C. D. Good, and R. Turner, "RF inhomogeneity compensation in structural brain imaging," *Magn Reson Med*, vol. 47, pp. 398-402, 2002.

[16] A. Haase, J. Frahm, D. Matthaei, W. Hanicke, and K. D. Merboldt, "Flash Imaging - rapid NMR imaging using low flip-angle pulses," *J Magn Reson*, vol. 62, pp. 258-266, 1986.

[17] J. P. Mugler and J. R. Brookeman, "3-Dimensional magnetization-prepared rapid gradient-echo imaging (3D MP-RAGE)," *Magn Reson Med*, vol. 15, pp. 152-157, 1990.

[18] F. Bloch, W. W. Hansen, and M. Packard, "The nuclear induction experiment.," *Phys. Rev.*, vol. 70, pp. 460-474, 1946.

[19] E. M. Purcell, H. C. Torry, and R. V. Pound, "Resonance absorption by nuclear magnetic moments in solid," *Phys. Rev.*, vol. 69, pp. 37, 1946.

[20] P. C. Lauterbur, "Image formation by induced local interactions; examples employing nuclear magnetic resonance," *Nature*, vol. 242, pp. 190-191, 1973.

[21] E. M. Haacke, R. W. Brown, M. R. Thompson, and R. Venkatesan, *Magnetic Resonance Imaging: Physical Principles and Sequence Design*: Wiley, 1999

[22] Z. P. Liang and P. C. Lauterbur, "Principles of Magnetic Resonance Imaging: A signal Processing Approach," 2000.

[23] D. I. Hoult, "The principle of reciprocity in signal strength calculations - A mathematical guide," *Concepts Magn Reson*, vol. 12, pp. 173-187, 2000.

[24] J. P. Wansapura, S. K. Holland, R. S. Dunn, and W. S. Ball, "NMR relaxation times in the human brain at 3.0 tesla," *J Magn Reson*, vol. 9, pp. 531-538, 1999.

[25] J. Szumowski and J. S, "Fat and water signal separation methods," in *Magnetic resonance imaging*, D. D. Stark and W. G. Bradley, Eds., 3rd Ed. ed. St. Louis: Mosby, 1999, pp. 162.

[26] H. E. Cline, W. E. Lorensen, R. Kikinis, and F. Jolesz, "Three-Dimensional Segmentation of MR Images of the Head Using Probability and Connectivity," *JCAT*, vol. 14, pp. 1037-1045, 1990.

[27] http://www.fmrib.ox.ac.uk/fsl/

[28] E. M. Haacke, R. W. Brown, M. R. Thompson, and R. Venkatesan, *Magnetic Resonance Imaging: Physical Principles and Sequence Design*: Wiley, 1999, pp. 877.